Structural damage detection using digital video imaging technique and wavelet transformation

U.P. Poudel, G. Fu*, J. Ye

Center for Advanced Bridge Engineering, Civil and Environmental Engineering Department, Wayne State University, 5050 Anthony Wayne Drive, 2157, Engineering Building, Detroit, MI 48202, USA

Abstract

Damage in structures may render risk of catastrophic failure. Identifying damages and their locations is termed as damage detection. In this paper, use of digital video imaging is proposed for detecting damage in structures. The theory of measuring structural vibration using high-resolution images is presented first, based on sub-pixel edge identification. Then a concept of mode shape difference function is developed for structural damage detection. A laboratory test program was carried out to implement these concepts using a high-speed digital video camera. The images were analyzed to obtain displacement time series at sub-pixel resolution. Mode shapes were obtained from the time series to find the mode shape difference functions between the damaged and the reference states. They were subjected to wavelet transformation for determining the damage locations. Results show that the proposed approach is able to identify the introduced damage cases and their locations.
© 2004 Elsevier Ltd. All rights reserved.

1. Introduction

Many structures in the civil infrastructure system need constant monitoring for deciding on repair, maintenance, and rehabilitation. Research efforts have been reported in the past for monitoring these structures using their dynamic characteristics [1], such as the natural frequencies and mode shapes.

---

*Corresponding author. Tel.: +1 313 577 3811; fax: +1 313 577 3881.
  E-mail address: upendra@wayne.edu (G. Fu).

Previously proposed approaches overwhelmingly used accelerometers for measurement, attached to the structure at a limited number of points. The effectiveness of these approaches still needs to be demonstrated because the resolution of the acquired data is limited. Such approaches also require access to the structure, which may be costly or impractical. To circumvent these difficulties, dynamic digital imaging is proposed here for structural health monitoring. Aspects related to this approach are briefly reviewed next, before it is fully presented later.

Damage and alteration to structures change their behaviors. If these changes are accurately measured, they can be used to identify and locate the structural damage and alteration. This process of identification is referred to as damage detection. Such detection should cover at least two key aspects: (1) detecting presence of damage, and (2) identifying the damage locations or neighborhoods. Doebling et al. [1] presented a literature review for damage detection of civil structures using vibration measurement, and Dimarogonas [2] for vibration-based methods for detecting cracks in particular. A number of previously proposed methods require a comprehensive dynamic analysis of the structure including a finite element analysis. This analysis is meant to establish a reference to be compared with measured results for damage identification. There are two main issues associated with this approach. (1) It is not always cost-effective to conduct dynamic analysis of a structure. (2) It is always very costly, if not impossible, to obtain valid models of finite element analysis for as-built civil structures. Without physical testing, the validity of these models cannot be confirmed.

During the last two decades, structural dynamic system parameters such as natural frequencies, damping, and mode shapes have been investigated for their possible use in structural damage identification and localization. While changes in natural frequencies may be used to detect the existence of damage, the mode shapes are more important indices for damage location identification. However, measurements using traditional sensors, such as accelerometers, offer low spatial resolution for mode shapes, because spatially intensive instrumentation would be costly. For this reason, digital imaging is considered in this research.

Digital imaging along with image analysis has been used for various applications as monitoring tool, such as machine tool condition monitoring [3], quality control inspection of electrical devices [4], visual inspection of computer integrated manufacture [5], identification of road curvature and vehicular motion [6], and automatic vision system for steel quality inspection [7]. Furthermore, computer vision has been used for automated defect classification for semiconductor chips [8], and for detecting and tracking road edges from images [9].

The information on the movement of an imaged object can be obtained by accurately identifying the object's boundaries in subsequent video images. These boundaries are called edges and their determination is referred to as edge detection. Depending on the accuracy requirement, edge detection may be done at pixel or sub-pixel level. Previously proposed edge detection procedures at pixel level may be categorized as follows. (1) Fitting the image data with a predefined model to extract edge information [10,11]. (2) Applying an edge operator or filter to the image data to identify the edge [12–17]. (3) Equalizing the theoretical spatial moments of an image model to those of the image data and then solving for the model's parameters [18]. (4) Determining the zero crossing of the image data subjected to the Laplacian of Gaussian mask as the edge's location [19,20]. (5) Applying the fuzzy set concept to estimate the edge parameters [21,22]. Edge detection at pixel level is not sufficient for the precise measurement required here, since it yields only integer values of pixels as the edge location.

Edge detection algorithms at sub-pixel level use information from neighboring pixels to determine the edge location within a pixel [23]. Typical approaches of sub-pixel edge detection are as follows. (1) Fitting a predetermined edge model to the image data [24]. (2) Convolving image data with predefined filters having sub-pixel accuracy [25]. (3) Non-linearly interpolating the image data [26]. (4) Equalizing spatial moments of a selected edge model and the image data to solve for the edge parameters in the model [27]. However, these previously proposed approaches still do not meet the resolution requirement for civil structural health monitoring and damage detection. The work reported in this paper attempts to address this issue, by developing a new edge detection algorithm at sub-pixel level for high accuracy.

For damage presence detection and their location determination, previous research efforts have been reported that use the difference between the mode shape's derivatives of intact and damaged (cracked) states of the structure, which result in spikes at the location of damage [28–31]. It is inferred that lower modes can be more useful than higher ones in such application [32]. However, for using the mode shape's derivatives, the measured data need to have high spatial resolution and low noise for reliable estimation of damage location. Hence, the difference in mode shapes for the damaged and reference states is to be used here in damage location identification, because mode shapes are less sensitive to noise.

Recently, wavelet transformation has found wider application in decomposing data to localize and zoom in their local characteristics [33,34]. A review is provided by Peng and Chu [35] of available wavelet transformation methods and their application to machine condition monitoring. Liew and Wang [36] found that crack location could be indicated by the variation of some wavelet coefficients along the length of a structural component. Furthermore, Wang and Deng [37] and Quek et al. [38] demonstrated the potential of Haar Wavelet transformation for damage detection. Hong et al. [39] presented damage detection for a beam structure using the Lipschitz exponents estimated by wavelet transform. The magnitude of Lipschitz exponent was used as an indicator of damage extent. Both numerical and experimental verification were shown utilizing the continuous Mexican Hat Wavelet transformation having two vanishing moments for determining the Lipschitz exponent. It was concluded that the first mode shape is more useful than higher ones in the exponent estimation and thus in detecting damage. Lu and Hsu [40] presented a wavelet transform-based method for the detection of structural damage, by comparison of the discrete wavelet transforms of the signals before and after damage in the spatial domain.

In this paper, video imaging is used for data acquisition for structural damage detection. A new edge detection algorithm is developed for highly accurate displacement measurement. Then a mode shape difference function is introduced and is experimentally obtained from the mode shapes of the reference and damaged states. The wavelet transformation is applied to the resulting mode shape difference function for diagnosis. This approach offers the advantage of spatially intensive vibration measurements, leading to higher resolution in damage location identification.

The scope of this research was the development of structural health monitoring technique for highway bridges, many of which are beam type structures. 3D digital imaging along with 3D edge detection is being investigated for determining the coordinate of the point of interest in the structure [41]. There is strong possibility of this method becoming applicable to a complex structure, if the damage in a complex structure changes its global dynamic behavior. Furthermore, if the complex structure permits to have its image taken from three or more angles, then the structures' 3D coordinates are determined from the image. Hence, the employment of three or

more digital video camera from different angles to image the structure with a simultaneous trigger mechanism gives a 3D measurement for the complex structure. With subsequent image analysis 3D coordinates of the structure in movement can be obtained which in turn provide time series information. The rest of the procedure remaining the same, such as modal analysis, mode shape extraction and further post-processing of such information using tools like wavelet transformation should make this method applicable to complex structures.

2. Theoretical developments

2.1. Image formation and sub-pixel edge detection

In digital images, objects may be identified using their outlines or edges. Typically, an edge in a monochrome image is located as a sharp change in the gray level. This change typically occurs over a number of neighboring pixels. Depending on the edge's characteristics several models have been proposed to describe them. The most popular ones are the step-, roof-, and ramp-edges [42]. Edges also convey information on the scene content, which is also used to identify the imaged environment in human visual systems. To realistically model edges for identifying them, it is important to understand the process of image formation. In the following section, the image formation process in a digital camera is discussed along with presenting the proposed sub-pixel level edge identification.

An ideal 1D step edge at location d on the x-axis can be defined as

$$W(x) = h + k\theta(x - d), \tag{1}$$

where $W(x)$ is the intensity level, h the background intensity, k the step height or edge contrast, and θ the unit Heaviside function, as shown in Fig. 1.

The edge in Eq. (1) is never imaged as an ideal edge. As outlined in Fig. 2, the image formation process involves optical blurring, digitization, and noise generation and addition to the image. They result in deviation from the ideal step edge function. Hence, recorded blurred edges are modeled here as the convolution of the ideal step function (Eq. (1)) with an impulse response
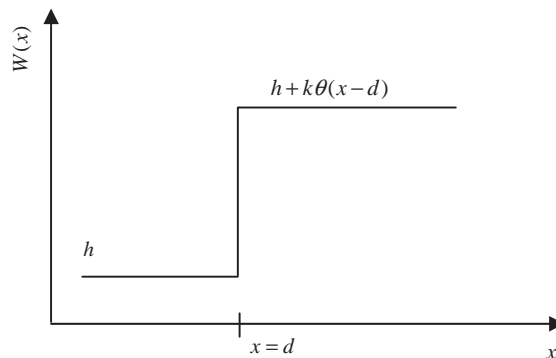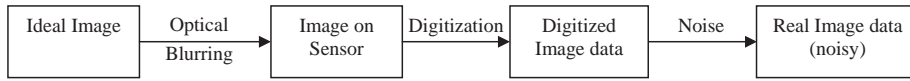

Fig. 1. 1D ideal edge (edge location at $x = d$).

Fig. 2. General image formation process.

function, the normal probability density function with variance a^2 defined as follows:

$$W'(x) = \int_{-\infty}^{\infty} (h + k\theta(x - d - t)) \left(\frac{1}{\sqrt{2\pi a}} e^{-t^2/2a^2} \right) dt$$
$$= h + k\Phi_a(x - d),$$ (2)

where $\Phi_a(x - d)$ is the cumulative probability function for the normal variable with mean d and variance a^2. $W'(x)$ represents the distribution of the light intensity received by the imaging sensor. Accordingly each pixel i's gray level $G(i)$ is modeled as a result of photon accumulation:

$$G(i) = \int_{i-1/2}^{i+1/2} (h + k\Phi_a(x - d)) \, dx.$$ (3)

Eqs. (1)–(3) can be readily extended to the 2D situation using a second-order polynomial for the edge:

$$W'(x, y) = h + k\Phi_a(y - (Px^2 + Qx + R)),$$ (4)

where $2P$ is the edge curvature, Q the edge slope at $x = 0$, R the y intercept (edge location at $x = 0$), a the blurring factor, h the intensity level of background, and k the difference of intensity over the edge (i.e., contrast).

Accordingly, the gray level $G(i, j)$ is modeled as a result of an accumulation process as follows:

$$G(i,j) = \int_{j-0.5}^{j+0.5} \int_{i-0.5}^{i+0.5} W'(x, y) \, dx \, dy \, (-I \leqslant i \leqslant I, \ -J \leqslant j \leqslant J),$$ (5)

where i and j are identification indices of the pixel. Fig. 3 depicts an example of gray level distribution according to Eq. (5). The parameter values for P, Q, R, h, k, and a are also shown in the figure, along with the ranges I and J for i and j (from –100 to + 100 for both). The ranges I and J in the two perpendicular directions define a window of the image used for edge identification computation.

In order to determine the six edge parameters (P, Q, R, h, k, and a) for identifying the edge location, slope, and curvature, a least-square curve fitting algorithm is proposed here as an optimization process. The objective function Δ to be minimized is defined here as the difference of the gray levels in the real image and generated according to the edge model

$$\Delta = \sum_i \sum_j [G(i,j) - \tilde{G}(i,j)]^2 \, (-I \leqslant i \leqslant I, \ -J \leqslant j \leqslant J),$$ (6)

where $G(i, j)$ is the gray level according to the model (Eq. (5)) with the six parameters to be identified, and $\tilde{G}(i,j)$ is the gray level in the real image. The solution procedure is given in Appendix A, which takes the advantage of closed-form derivatives of the objective function Δ with respect to the edge parameters (P, Q, R, h, k, and a). This approach was taken to minimize
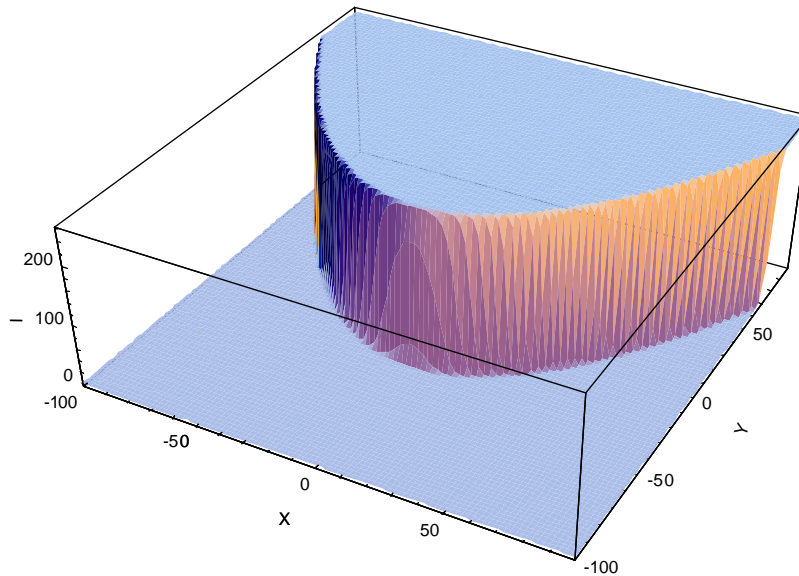
Fig. 3. 2D edge model of light intensity ($P = 0.01$, $Q = 0.01$, $R = -30.00$, $h = 0.00$, $k = 256.00$, $a = 1.00$).

the computation time. It also maximizes the solution's accuracy because it eliminates numerical differentiation that is sensitive to noise.

2.2. Vibration time series from sequence of images

A digital video camera can form a sequence of images to record an object's motion. Due to commercial availability of high-speed digital video cameras (up to 40,000 frames/s at present), typical mechanical oscillation can be readily captured. Then, time series of the vibrating object can be obtained using image processing techniques. The edge identification method presented above has high resolution and accuracy for this purpose. The following procedure is used here for time series information extraction, and is also shown in the flowchart of Fig. 4: (1) Acquire images of a scale object (with known dimensions) along with the object whose motion is to be measured. Extract edge information (location, slope, and curvature) in the obtained images for the scale object and determine the scaling factor (in length per pixel). (2) Acquire baseline images of the interested object not in motion, and extract edge information from them. (3) Take images when the interested object is in motion, and extract edge information from the motion images. (4) Find the object's relative motion by subtracting the baseline edge information (from Step (2)) from the motion edge information (from Step (3)). Repeat this step for all images. (5) Multiply the scaling factor to the result of Step 4 to obtain motion time series in proper dimensional unit.

2.3. Mode shape difference function

The mode shapes of a structure describe the relative motion relationship of various points of the structure. When damage occurs at one or more of these points, this relative relationship will
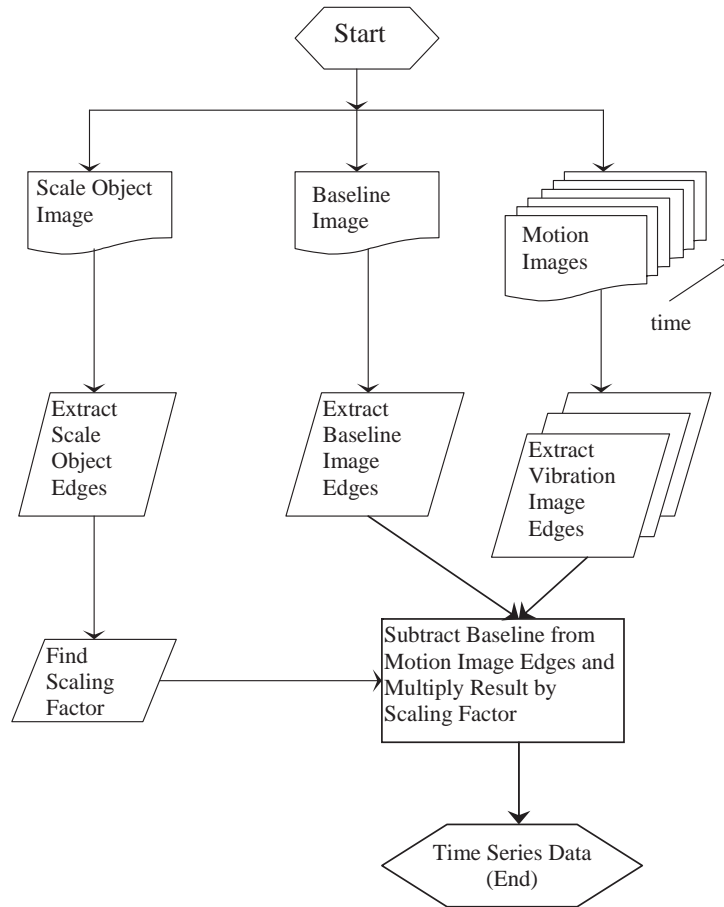
Fig. 4. Time series extraction process.

change. This change is used here for damage detection, focusing on the difference of the mode shapes before and after structural damage.

For ease of demonstration, a simply supported prismatic beam is considered here, using its intact and damaged states. It is assumed that the beam's mass remains constant after damage and only the structure's stiffness is changed due to the damage. Let $\bar{m}$ be the constant mass. The flexural stiffness of the beam is a constant $E\bar{I}_0$ when the beam is intact, and $EI_0(x)$ when it has a crack. The stiffness of the damaged beam is modeled as follows, including a crack:

$$EI(x) = E\bar{I}_0\left(1 - Ce^{-(x-\alpha/\sigma)^2}\right), \tag{7}$$

where α, C, and σ are, respectively, the crack's location, depth ratio, and characteristic width, and x is measured from the left support. E and $\bar{I}_0$ are the Young's modulus and the intact moment of
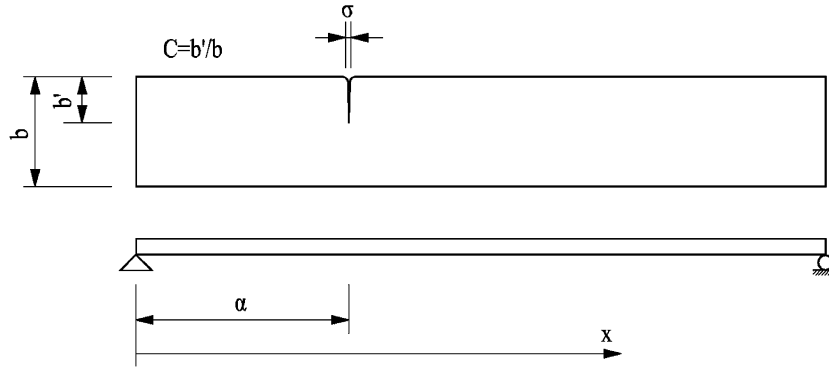
Fig. 5. Schematic diagram of damaged beam.

inertia of the beam. A schematic diagram of Eq. (7) is shown in Fig. 5 for a damaged beam. The purpose of using the continuous function in Eq. (7) to model a supposedly discontinuous crack is to allow a closed form solution. For very small cracks, the solution may be used with the characteristic width approaching to zero. The equation of free vibration motion for the beam is written as follows considering only the flexural effect:

$$\frac{\partial^2}{\partial x^2}\left[EI(x)\,\frac{\partial^2 v(x,t)}{\partial x^2}\right] + \bar{m}\,\frac{\partial^2 v(x,t)}{\partial t^2} = 0, \tag{8}$$

where $v(x,t)$ is the displacement of the beam perpendicular to its axis, at location x for time t. Separating the temporal and spatial variables as follows can help readily solve this equation:

$$v(x,t) = \phi(x)Y(t), \tag{9}$$

where $Y(t)$ is a function of time, and $\phi(x)$ is the mode shape function. The latter has the form in Eq. (10) for the intact state and Eq. (11) for the two segments of the damaged beam separated by the crack, respectively:

$$\phi(x) = A_1 \cos \lambda x + A_2 \cosh \lambda x + A_3 \sin \lambda x + A_4 \sinh \lambda x \tag{10}$$

$$\begin{aligned}
\phi_1(x) &= A_{11} \cos \lambda x + A_{12} \cosh \lambda x + A_{13} \sin \lambda x + A_{14} \sinh \lambda x \quad \text{for} \quad 0 \leqslant x \leqslant \alpha \\
\phi_2(x) &= A_{21} \cos \lambda x + A_{22} \cosh \lambda x + A_{23} \sin \lambda x + A_{24} \sinh \lambda x \quad \text{for} \quad \alpha \leqslant x \leqslant L
\end{aligned} \tag{11}$$

where L is the length of the beam. The mode shapes are required to satisfy the following boundary conditions for the two states, respectively:

$$\phi(0) = 0, \quad \phi(L) = 0, \quad \left.\frac{\partial^2 \phi(x)}{\partial x^2}\right|_{x=0} = 0, \quad \left.\frac{\partial^2 \phi(x)}{\partial x^2}\right|_{x=L} = 0, \tag{12}$$

$$\phi_1(0) = 0, \quad \phi_2(L) = 0,$$

$$\left.\frac{\partial^2 \phi_1(x)}{\partial x^2}\right|_{x=0} = 0, \quad \left.\frac{\partial^2 \phi_2(x)}{\partial x^2}\right|_{x=L} = 0,$$

$$\phi_1(\alpha) - \phi_2(\alpha) = 0, \quad \left.\frac{\partial^2 \phi_1(x)}{\partial x^2}\right|_{x=\alpha} - \left.\frac{\partial^2 \phi_2(x)}{\partial x^2}\right|_{x=\alpha} = 0,$$

$$\left.\frac{\partial^3 \phi_1(x)}{\partial x^3}\right|_{x=\alpha} - \left.\frac{\partial^3 \phi_2(x)}{\partial x^3}\right|_{x=\alpha} = 0, \quad \left.\frac{\partial \phi_1(x)}{\partial x}\right|_{x=\alpha} - \left.\frac{\partial \phi_2(x)}{\partial x}\right|_{x=\alpha} = \frac{\sigma C}{1-C} L \left.\frac{\partial^2 \phi_2(x)}{\partial x^2}\right|_{x=\alpha}, \quad (13)$$

where $\lambda^4 = \omega^2 \bar{m}/(E\bar{I})$ with ω^2 being the natural frequency of the beam. Coefficients A_{1i} and A_{2i} ($i = 1, \ldots, 4$) in Eq. (11) can be solved using the boundary conditions in Eq. (13). This solution process results in a set of eight homogeneous linear algebraic equations for the eight unknown coefficients. Subsequently, the following natural frequency equation is obtained to have non-trivial solutions to the homogenous equations:

$$\sin \lambda L \sinh \lambda L + \frac{\sigma C L \lambda}{2(1-C)} (\sin \alpha\lambda \sin(\alpha - L)\lambda \sinh L\lambda$$

$$- \sin L\lambda \sinh \alpha\lambda \sinh(\alpha - L)\lambda) = 0. \quad (14)$$

As shown, the natural frequencies are functions of characteristic crack width σ, crack location α, and crack depth ratio C. Furthermore, using the obtained frequencies in the eight boundary conditions in Eq. (13) leads to the mode shapes

$$\phi_1(x) = A_{13}\left(\sin \lambda x + \frac{\sin \lambda L \sinh \lambda(L-\alpha)\sinh \lambda x}{\sin \lambda(L-\alpha)\sinh \lambda L}\right), \quad \text{for } 0 \leqslant x \leqslant \alpha$$

$$\phi_2(x) =$$

$$A_{13} \frac{\sin \lambda L\{\cosh \lambda(\alpha + L - x) - \cosh \lambda(\alpha - L + x)\} + \sinh \lambda L\{\cos \lambda(\alpha - L + x) - \cos \lambda(\alpha + L - x)\}}{2 \sin \lambda(L-\alpha)\sinh \lambda L},$$

$$\text{for } \alpha \leqslant x \leqslant L \quad (15)$$

Once the mode shapes for both the intact and damaged beams are known, their difference can be readily calculated as:

$$f(x) = \phi_1(x) - \phi(x), \quad \text{for } 0 \leqslant x \leqslant \alpha; \qquad f(x) = \phi_2(x) - \phi(x), \ \text{for } \alpha \leqslant x \leqslant L. \quad (16)$$

This mode shape difference function has a maximum magnitude at the location of damage or discontinuity. A numerical example of this function is shown in Fig. 6 for the first mode of a 100 cm long beam having $C = 10\%$ at the locations indicated. It is seen that the mode shape difference functions reach the maximum values at the crack locations.

In practical applications, the reference state may not be the intact state. For such a situation Fig. 7 shows the mode shape difference functions between two damage states. They are (1) damage at $\alpha = 30$ cm and (2) damage at both $\alpha = 30$ cm and $\alpha = 70$ cm. For reference, each damage state's mode shape difference function compared with the intact state is also shown. It is seen that the mode shape difference function between the damage state with $\alpha = 30$ cm and the intact state has one maximum at the damage location. For the case of $\alpha = 30$ and 70 cm the function has two peak values corresponding to the two damage locations. The same function
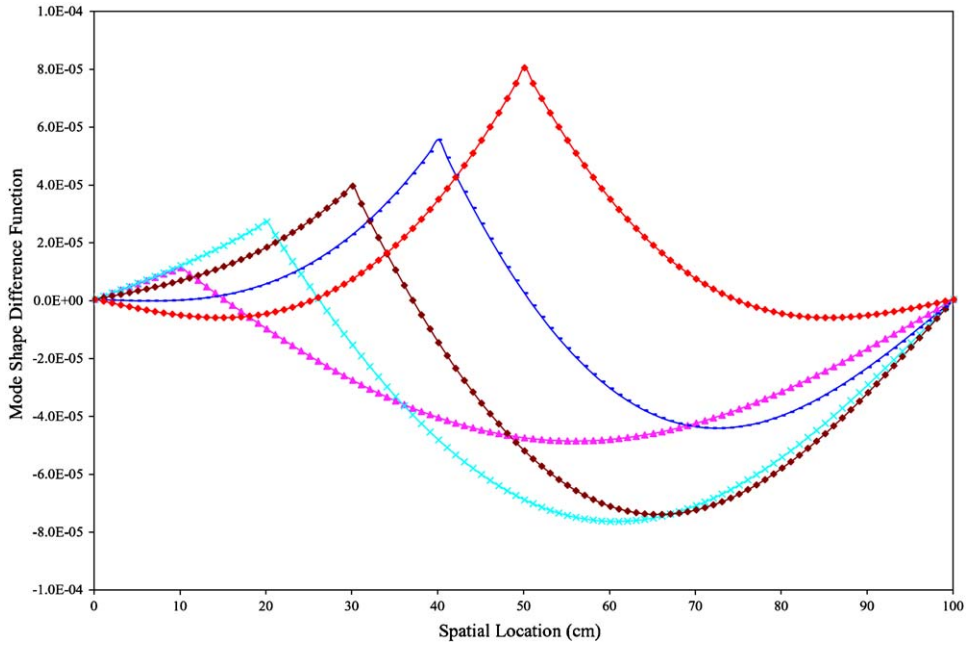
Fig. 6. Analytical first mode shape's difference functions between intact and damaged beams: $C = 10\%$, $\sigma = 0.001$, and α as $-\blacktriangle-$, 10 cm; $-\times-$, 20 cm; $-\blacklozenge-$, 30 cm; $—\cdot—$, 40 cm; and $-\blacklozenge-$, 50 cm.

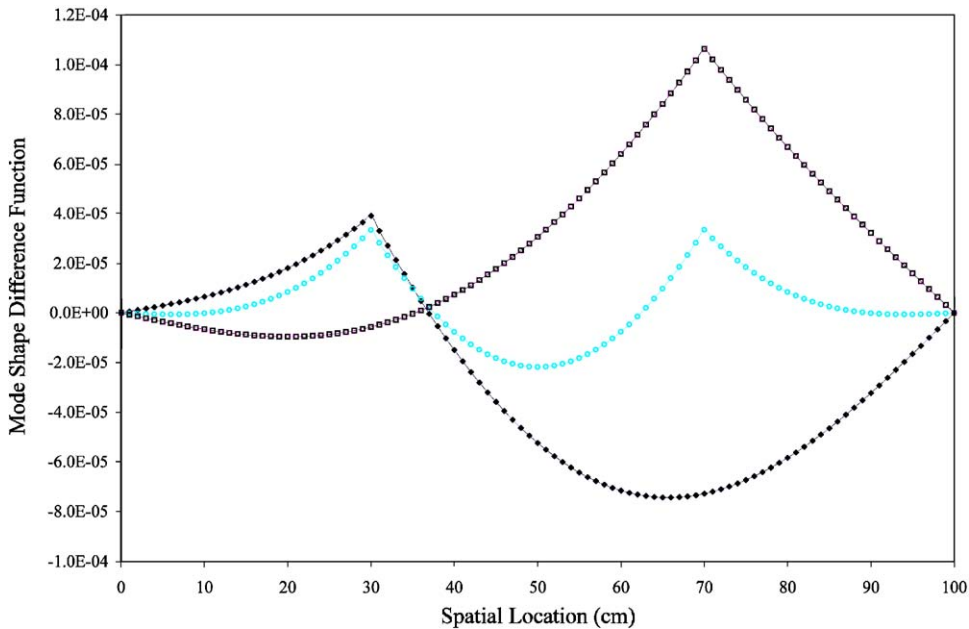
Fig. 7. Analytical first mode shape's difference functions between two states ($C = 10\%$, $\sigma = 0.001$), for: $-\blacklozenge-$, damage at 30 cm vs. intact; $—\circ—$, damage at 30 and 70 cm vs. intact; and $-\square-$, damage at 30 and 70 cm vs. damage at 30 cm.
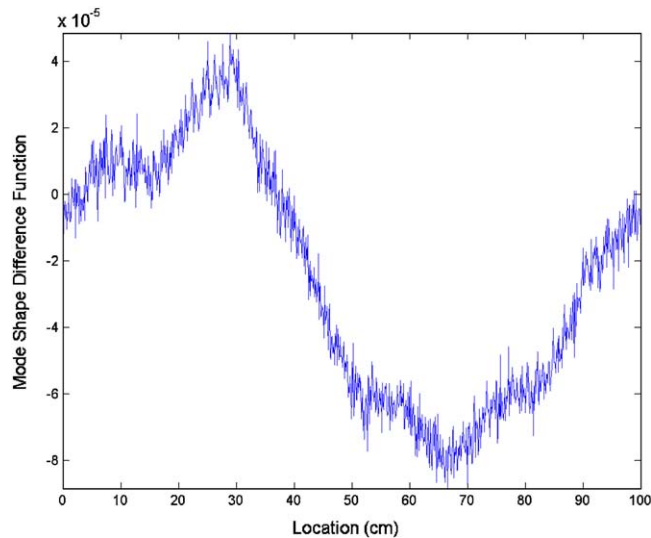
Fig. 8. Synthetic noisy mode shape difference function ($C = 10\%$, $\alpha = 30\,\text{cm}$).

between the two damage cases has only one peak at $\alpha = 70\,\text{cm}$ since the damage at $\alpha = 30\,\text{cm}$ has not changed.

Note also that noise is inevitable in experimental data. To demonstrate the effect of noise on mode shape difference function, Fig. 8 shows a synthetic noisy mode shape difference function for $C = 10\%$ and $\alpha = 30\,\text{cm}$. The noise is Gaussian and has a standard derivation equal to 20% of the function's average. It is also periodic with 6 cycles over the beam length.

Moreover, applicability of the mode shape difference function for a plate type structure is explored for a simply supported steel plate ($50\,\text{cm} \times 50\,\text{cm} \times 1.5\,\text{cm}$). Intact state and damaged state ($0.50\,\text{cm} \times 0.50\,\text{cm} \times 0.50\,\text{cm}$ damage at $x = 16.5\,\text{cm}$, $y = 25\,\text{cm}$) mode shapes were obtained using the ABAQUS® finite element program. The mode shape difference function is obtained for the first mode shape of plate structure and is shown in Fig. 9, which affirms the applicability for plate type structures.

2.4. Wavelet transformation and damage detection

The classical Fourier transformation portrays a signal record as superposition of infinite sinusoidal waveforms of assorted frequencies representing an orthogonal basis. Due to the fixed frequency basis used, the Fourier decomposition is suitable for signal records having relatively stationary frequency characteristics throughout their entire length. On the other hand, the wavelet transformation uses special sets of basis that are localized both in the original (e.g., the time) and the transformed (e.g., the frequency) domains [33,43–46]. Hence, the wavelet transformation is more suitable for analyzing non-stationery signal records, such as those with discontinuities or sudden (i.e., local) changes. The mode shape difference function defined in Eq. (16) is seen to have such local changes at the damage locations. They can be more effectively identified using wavelet transformation.
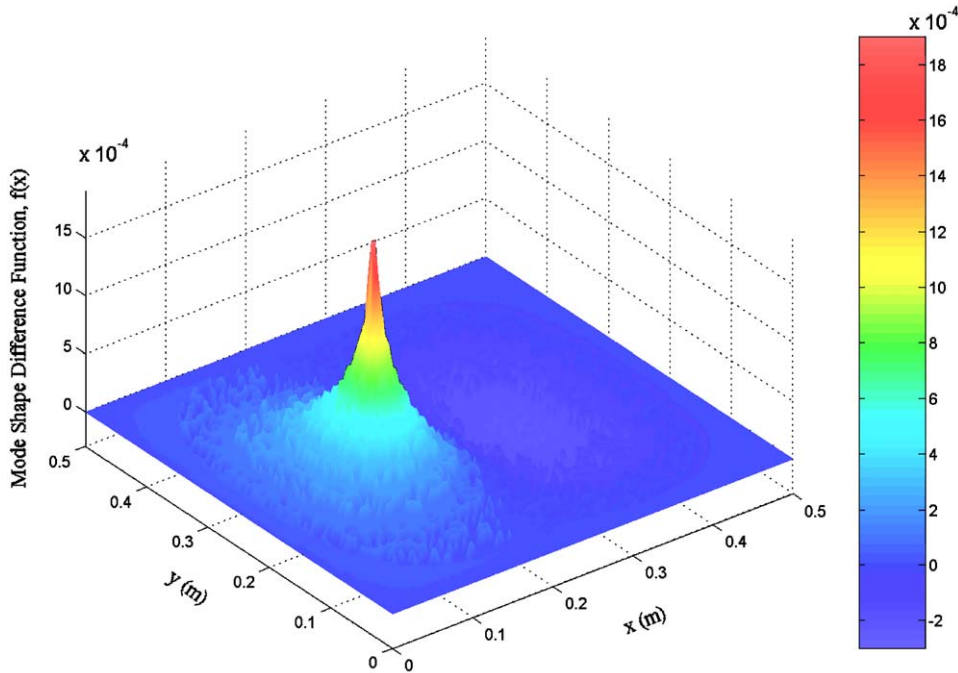
Fig. 9. Analytical first mode shape's difference function between damaged and intact simply supported plate of 50 cm × 50 cm × 1.5 cm size (0.50 cm × 0.50 cm × 0.50 cm damage at $x = 16.5$ cm, $y = 25$ cm).

The orthonormal basis function for wavelet transformation can be expressed as:

$$g(s, c, x) = \frac{1}{\sqrt{s}} \, \Psi\left(\frac{x - c}{s}\right), \tag{17}$$

where s is a scale parameter, c the translation parameter, and Ψ the mother wavelet function satisfying the conditions of zero mean, finite energy (i.e., finite L_2 norm), and band passing, i.e., the frequency response decays sufficiently rapidly as $\omega \to \infty$ and is zero as $\omega \to 0$ [47]. Note that both wavelet and Fourier transformations can be viewed as mapping the signal record in one space to another. A major difference between them, because of the different basis functions used and the flexibility of the wavelet transform, is that the wavelet transformation is able to localize non-stationery behavior that cannot be easily portrayed by Fourier transformation. For the application of structural damage detection, the wavelet transformation is advantageous. It is because the transformation window can vary by adjusting s and c in Eq. (17) to isolate and identify possibly different discontinuities or non-stationery behaviors in the signal record in different resolutions. These behaviors are due to structural damages and therefore they can be used to detect the damage locations.

In this study, the wavelet transformation is used to analyze signal records in the spatial domain x. Thus the transformed domain of s represents spatial period. Without loss of generality, consider a spatial signal $f(x)$, e.g., as defined in Eq. (16) over the space $x \in [0, L]$. The wavelet

transform for the signal record is defined in the same domain as

$$\psi(s, c) = \int_0^L f(x)\overline{g(s, c, x)}\, dx, \tag{18}$$

where $\psi(s, c)$ is the transformed wavelet coefficients for scale parameter s and translational parameter c, and $\overline{g(s, c, x)}$ is the conjugate function of $g(s,c,x)$ defined in Eq. (17).

For detecting local changes in $f(x)$, it is important to choose an appropriate mother wavelet Ψ, i.e., able to easily portray the changes and also not very sensitive to data noise. In this regard continuous transformation is advantageous to discrete transformation since it allows both the scale and translation parameters to vary in a continuous manner. Furthermore, a mother wavelet function is effective if it is able to portray discontinuity in the derivatives of $f(x)$ in the original and transformed domains. Hence, the continuous complex Gaussian wavelet is selected here:

$$\Psi(x) = D_n \frac{\partial^n (e^{-ix} e^{-x^2})}{\partial x^n}, \tag{19}$$

where $i = \sqrt{-1}$, n indicates the order of the wavelet, and D_n is a constant to make the second norm (L_2) of the function's nth derivative unity. Fig. 10 shows this wavelet function of second order ($n = 2$). Since the wavelet function is complex, the wavelet coefficient $\Psi(s, c)$ will be complex according to Eq. (18). One may use the wavelet coefficients in both the original (spatial location) and the transformed (spatial period) domains to determine damage location, corresponding to the locations of the wavelet coefficients' maxima modulus and change in phase angle. Fig. 11 shows
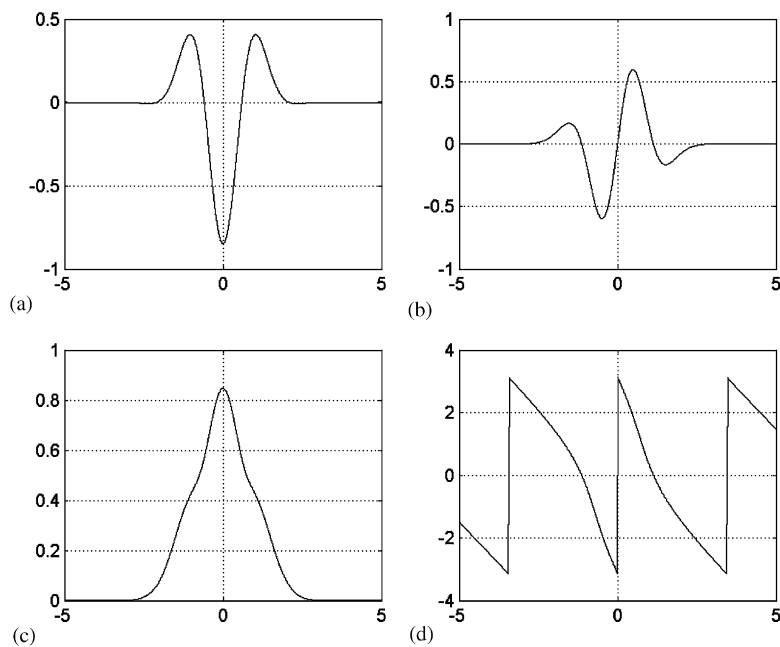

Fig. 10. Second order complex Gaussian function Ψ (Eq. (19)) in effective support width of $[-5,5]$ ($c = 0$, $s = 1$): (a) real part, (b) imaginary part, (c) modulus, and (d) phase angle of function.

the wavelet coefficients as functions of translation and scale parameters c and s for the mode shape difference function defined in Eq. (16) and plotted in Fig. 6, with $C = 10\%$, $\alpha = 30$ cm, and $\sigma = 0.0001$. Fig. 11(a) and (b) show the real and imaginary parts of $\psi(s, c)$ defined in Eq. (18). Fig. 11(c) and (d) show the modulus and phase angle of the same function. They are displayed in the 3D format, with s and c as variables. Fig. 11(e), (g), and (i) show more details of the modulus for the given s values, and Fig. 11(f), (h), and (j) for the phase angle. Examining the modulus and the phase angle in Fig. 11(e)–(h), it is easy to determine the damage location, where the modulus reaches maximum and the phase angle changes its sign. When scale s becomes larger the effective support window of the wavelet $[-2.5s, 2.5s]$ can be beyond the spatial domain $[0, L]$. The resulting transform will not fully portray $f(x)$. This is referred to as edge influence. Note that effective support window is based on the total energy concentrations with respect to effective window size as described in Table 2. Fig. 11(i) and (j) show an example of significant edge influence, where the maximum modulus does not occur with phase angle sign change. These locations should not be diagnosed as the damage locations, which deserve attention in damage location identification.

Another important factor affecting diagnosis is noise in the measured data. To investigate this effect, Fig. 12 shows the wavelet transform for the same mode shape difference function but with noise given in Fig. 8. Comparison of Figs. 11 and 12 can help to identify the effect of noise. When there is noise, finer scales s less than 100 results in noisy details shadowing the real damage location, as shown in Fig. 12 (a)–(d). The high frequency noise is "filtered out" when s becomes large, as seen in Fig. 12(e)–(h), and the damage location can be readily identified there. Therefore it is important to decide which scale levels should receive attention in identifying damage location.

3. Application experiments and results

The proposed concept of structural damage detection using high-resolution images was experimented in the laboratory. A simply supported prismatic steel beam was used as a structural model, to provide vibration measurement data for its intact and damaged states. The beam is 15.24 cm wide, 0.635 cm thick, and 110.5 cm long. Two damage states were realized by saw cut with depth of 2.5 and 2.2 cm ($C = 16.40\%$ and 14.40% in Eq. (7)), respectively, at locations $\alpha = 34.3$ and 74.0 cm from the left support of the beam as defined in Fig. 5. The two damage states are referred to as D1 and D2, respectively. Note that state D2 actually included state D1, since the latter was not revoked when the second damage was introduced. The beam's free vibration was recorded using a video camera, excited by imposing an initial displacement at 45.0 cm from the left support. The digital motion images were captured using a Nac Memrecam fx K3 digital video camera. The camera has a CMOS sensor with a 1280×1024 resolution and a 10-bit A/D converter. The camera is equipped with a 1.3 GB onboard memory and its frame rate ranges from 100 to 2000 frames/s.

The test setup is shown in Fig. 13. The procedure shown in Fig. 4 was followed for image taking and processing. First, the baseline (not in motion) images along with the scale object were taken. In the vertical direction, intended to be the direction of measured vibration displacement, a scale object (with two white marks) was used to allow acquisition of the scaling factor. These images were used to determine the scaling factor as 0.0714502 cm/pixel. Then, the intact beam was excited and its free vibration motion was captured at a rate of 1000 frames/s for a 1-s duration. These
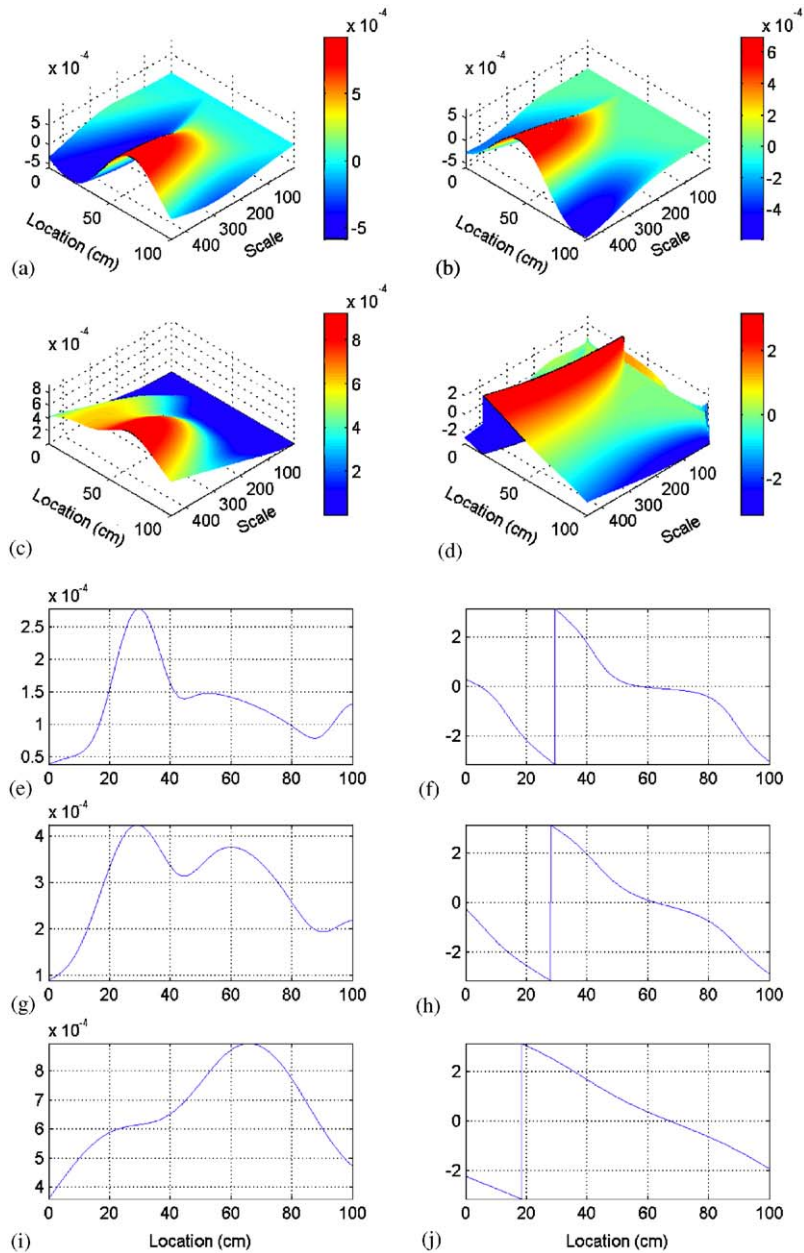
Fig. 11. Complex Gaussian wavelet coefficients of analytical mode shape difference function ($C = 10\%$, $\alpha = 30$ cm, and $\sigma = 0.001$): (a) real coefficients, (b) imaginary coefficients, (c) modulus of coefficients, (d) angle of coefficients, (e) modulus at $s = 133$, (f) angle at $s = 133$, (g) modulus at $s = 200$, (h) angle at $s = 200$, (i) modulus at $s = 400$, and (j) angle at $s = 400$.
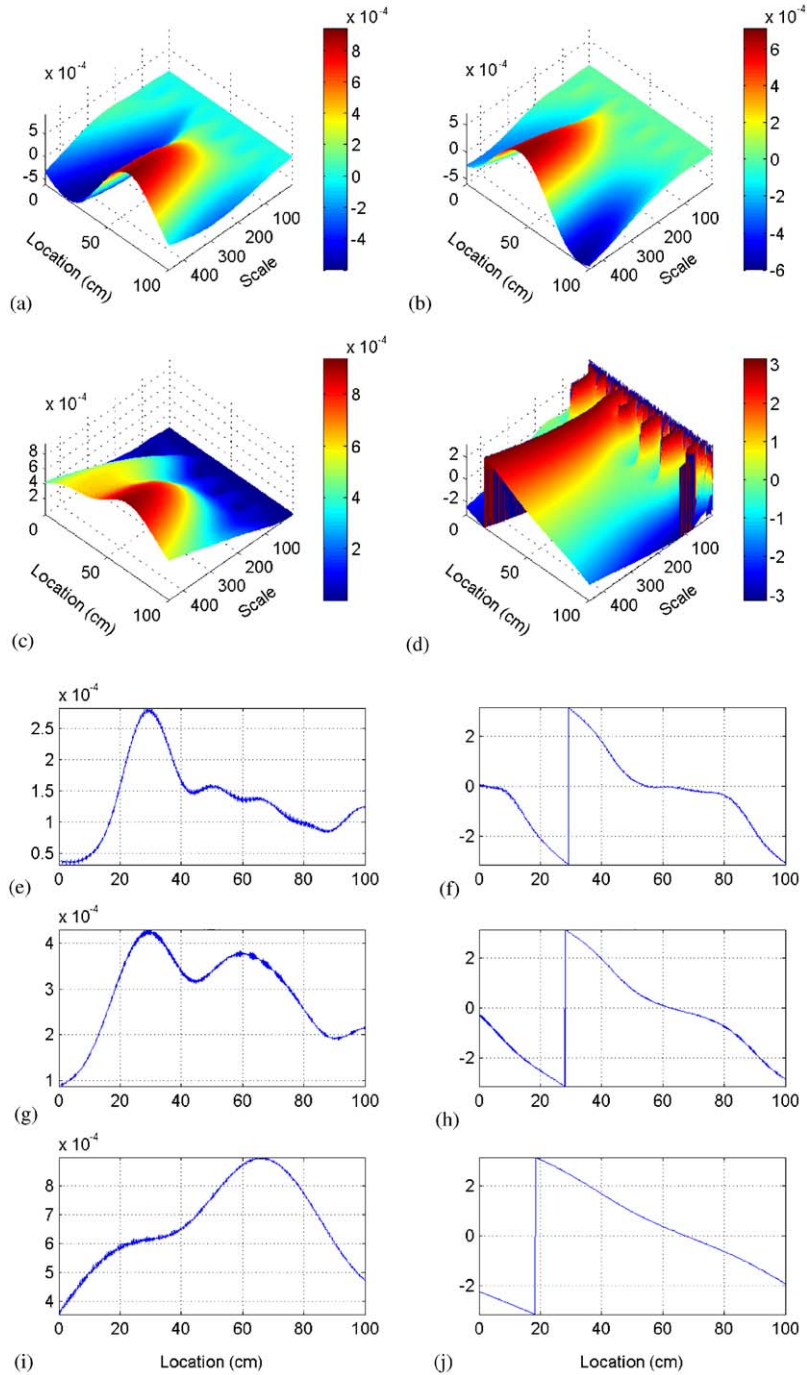
Fig. 12. Complex Gaussian wavelet coefficients of noisy analytical mode shape difference function of Fig. 8 ($C = 10\%$, $\alpha = 30$ cm, and $\sigma = 0.001$): (a) real coefficients, (b) imaginary coefficients, (c) modulus of coefficients, (d) angle of coefficients, (e) modulus at $s = 133$, (f) angle at $s = 133$, (g) modulus at $s = 200$, (h) angle at $s = 200$, (i) modulus at $s = 400$, and (j) angle at $s = 400$.

Fig. 13. Laboratory test setup.

images were processed using a personal computer for edge detection and displacement identification as presented earlier. The obtained time series of the beam in motion was used to extract dynamic properties for the intact beam. Then the beam was damaged using saw cut to its backside, so that the damage was not seen on the imaged front edge in edge identification. The same procedure was followed to obtain the time series of the beam with damage. A total of 16 sets of video were recorded each consisting of 1001 images. Eight sets were for the intact state and four for each of the two damage states.

The images were analyzed using the proposed sub-pixel edge identification procedure using a window size of $I = 50$ and $J = 7$ pixels for analyzing each available data point (pixel) along the beam length. The edge location, slope, and curvature of the beam were determined. Each image took about 5 min of processing time using a PIV IBM compatible PC with a 3.06 GHz microprocessor and a 1024 MB onboard memory. Fig. 14 shows a typical set of vibration time series for the intact beam. There are 1001 data points (i.e., images) in the time domain and 1131 data points in the spatial domain along the beam length. This time series shows that high-resolution video cameras are able to provide spatially intensive measurements, more cost-effectively than traditional sensors, such as dial gages, linear variable differential transformers (LVDT), and accelerometers.

The time series data from 1131 spatial points for 1-s duration were then processed using the MEscope Ves software [48] to obtain the natural frequencies, modal damping ratios, and mode shapes. Table 1 shows the first natural frequency and associated damping ratio for the intact and damaged states. Fig. 15 shows the corresponding mode shapes. Fig. 16 displays the mode shape difference function for the two damage cases, referring to different states as given in the legend Table 2.

The mode shape difference functions were then subjected to the second-order complex Gaussian wavelet transformation defined in Eq. (19) with $n = 2$, with scale s ranging from 1 to 512 pixels. The results are shown in Figs. 17–19. Smaller values of scale correspond to higher spatial
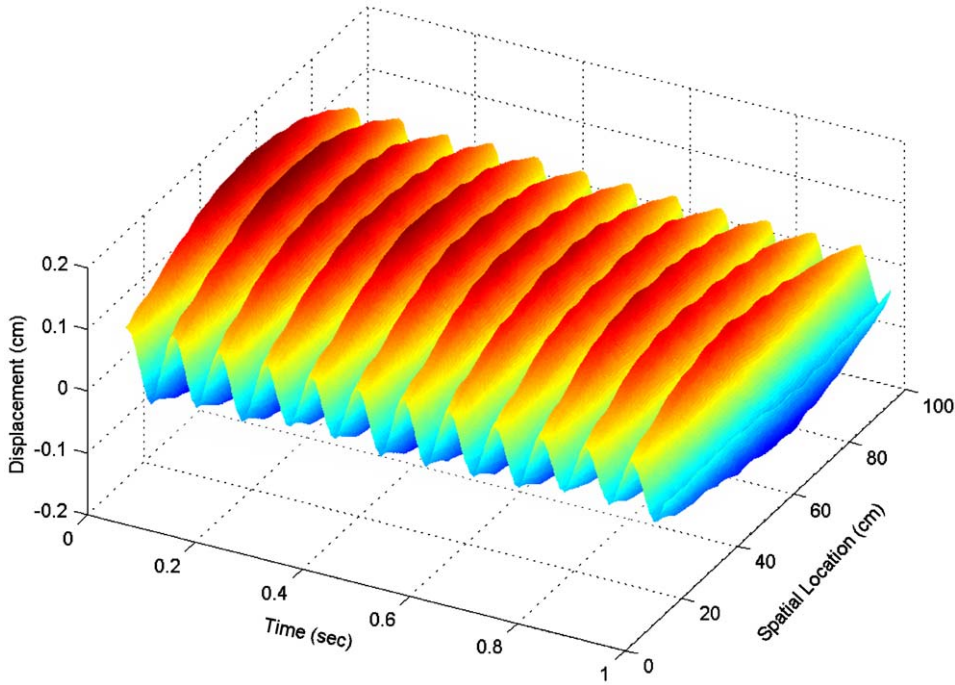
Fig. 14. Typical displacement time series for beam.

Table 1
First natural frequency and damping of intact and damaged beams

| Replicate ID | Undamaged state | | Damaged state | | | |
| | Frequency (Hz) | Damping (%) | D1 | | D2 | |
			Frequency (Hz)	Damping (%)	Frequency (Hz)	Damping (%)
1	11.738	0.32	11.575	0.39	11.459	0.36
2	11.755	0.41	11.592	0.40	11.454	0.33
3	11.737	0.38	11.573	0.39	11.466	0.38
4	11.74	0.38	11.609	0.45	11.478	0.43
5	11.757	0.40	—			
6	11.762	0.45				
7	11.757	0.43				
8	11.743	0.39				

frequencies (which are able to portray a higher number of discontinuities in the spatial domain along the beam length). In contrast, larger values of scale s correspond to lower spatial frequencies, useful for identifying a smaller number of changes or damage. Nevertheless, when the scale becomes large the edge influence also increases, as discussed earlier. The effective window for the mother wavelet function in Eq. (19) is about $5s + 1$ pixels. Thus the maximum s beyond which
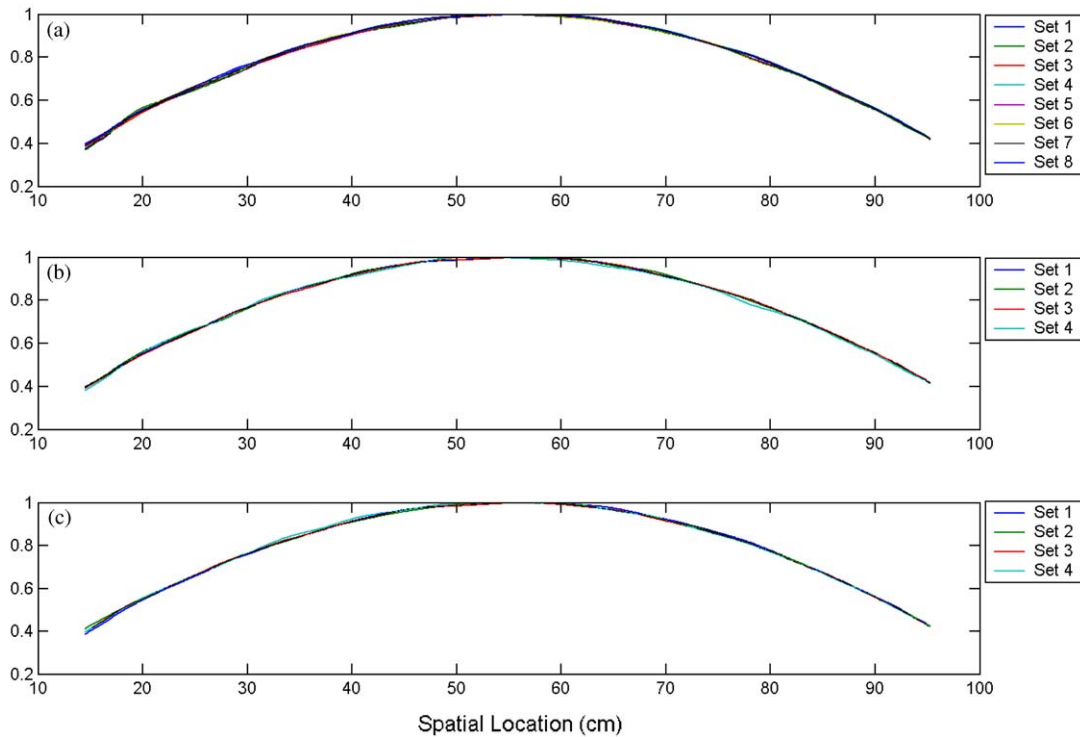
Fig. 15. First mode shapes for intact state and damage states: (a) intact state mode shape, (b) damage state (D1) mode shape, and (c) damage state (D2) mode shape.

the edge influence will be present can be found as $s < (N - 1)/5 \approx 226$, where N is the number of data point (1131). According to the discussion on data noise earlier, $s < 150$ should be also neglected considering the noise in the data. It is seen in Fig. 17(e)–(h) that the damage location can be identified at 33 cm with maximum modulus and sudden phase angle change. Note also that Fig. 17(i) and (j) show that the damage location is slightly shifted due to the edge influence.

Fig. 18 shows similar results for damage state D2 ($C = 16.40\%$ at $\alpha = 34.3$ cm and $C = 14.4\%$ at $\alpha = 74.0$ cm) referring to the intact state. The damage locations are identified at 30 and 78 cm where modulus maximum and phase angle sign change occur. If state D1 is used as the reference, Fig. 19 shows the result for state D2 for damage identification. Fig. 19(e)–(h) show the additional damage beyond state D1 at 78.75 cm, where both modulus maximum and phase angle sign change are observed.

4. Conclusions

A new approach to spatially intensive data acquisition is introduced and demonstrated here using a high-speed digital video camera. This non-contact method can be useful for structural damage detection when the structure is not easily accessible, which is often the case for civil
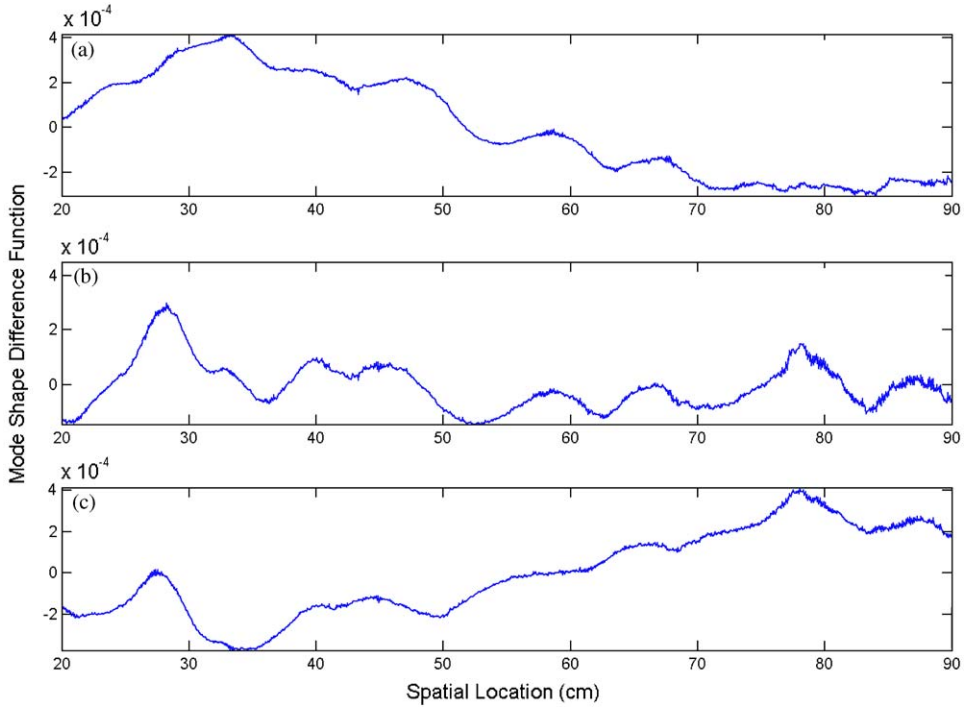
Fig. 16. First mode shape's difference functions between damaged and reference states: (a) damage state (D1) vs. intact, (b) damage state (D2) vs. intact, and (c) damage state (D2) vs. damage state (D1).

Table 2
Total energy concentrations with respect to effective window size

S. No.	Window size ($\pm$)	Energy percentage $\left(\frac{\int_{-s}^{s} \lvert\psi(x)\rvert^2 \mathrm{d}x}{\int_{-\infty}^{\infty} \lvert\psi(x)\rvert^2 \mathrm{d}x} \times 100\% \right)$
1	0	0
2	0.5	58.59
3	1.0	84.65
4	1.5	97.07
5	2.0	99.81
6	2.5	99.99
7	3.0	100.0
8	3.5	100.0
9	4.0	100.0
10	4.5	100.0
11	5.0	100.0

structures. The resulting spatially intensive data are much preferred over traditional point measurement data via, e.g., LVDTs and accelerometers. Using spatially intensive time series data and thereby derived data, mode shape difference between the reference and damaged state is
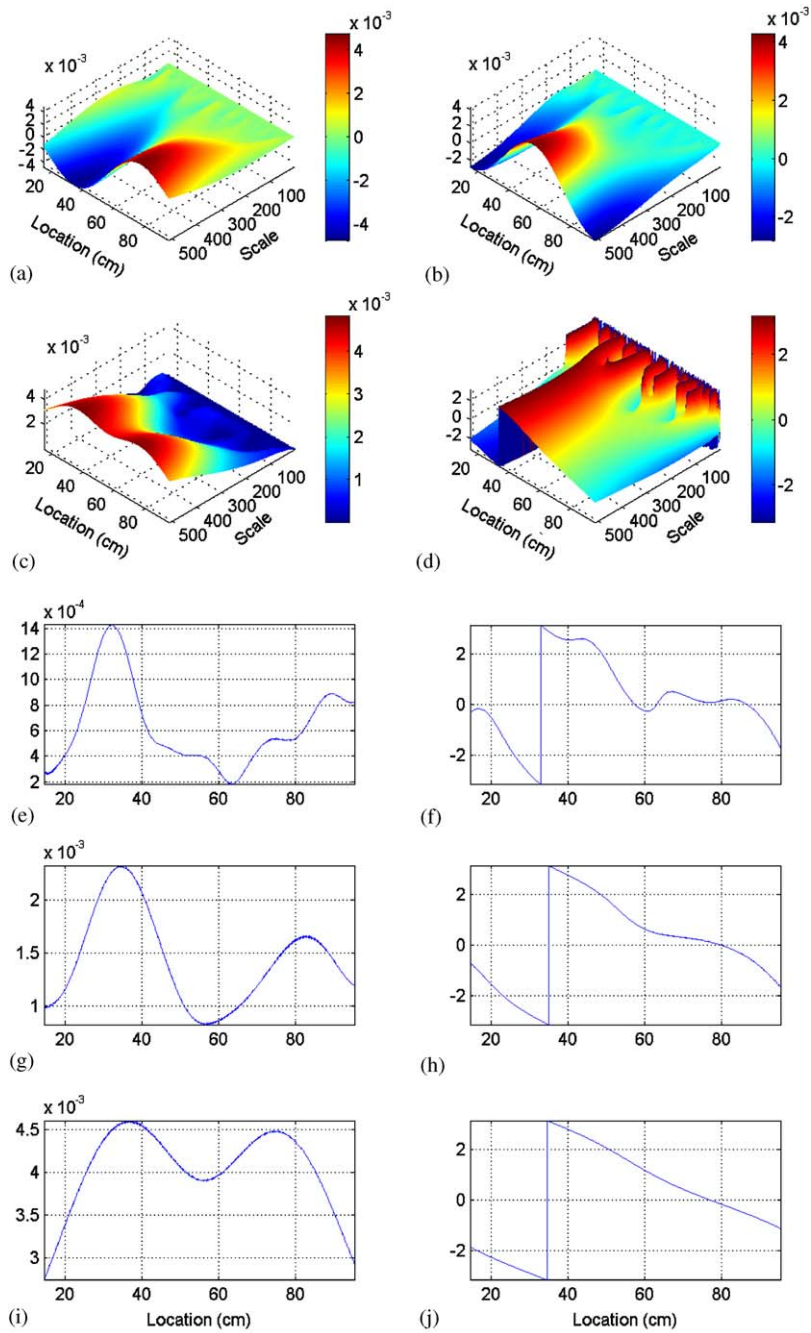
Fig. 17. Complex Gaussian wavelet coefficients of mode shape difference function between D1 and intact state: (a) real coefficients, (b) imaginary coefficients, (c) modulus of coefficients, (d) angle of coefficients, (e) modulus at $s = 150$, (f) angle at $s = 150$, (g) modulus at $s = 226$, (h) angle at $s = 226$, (i) modulus at $s = 452$, and (j) angle at $s = 452$.
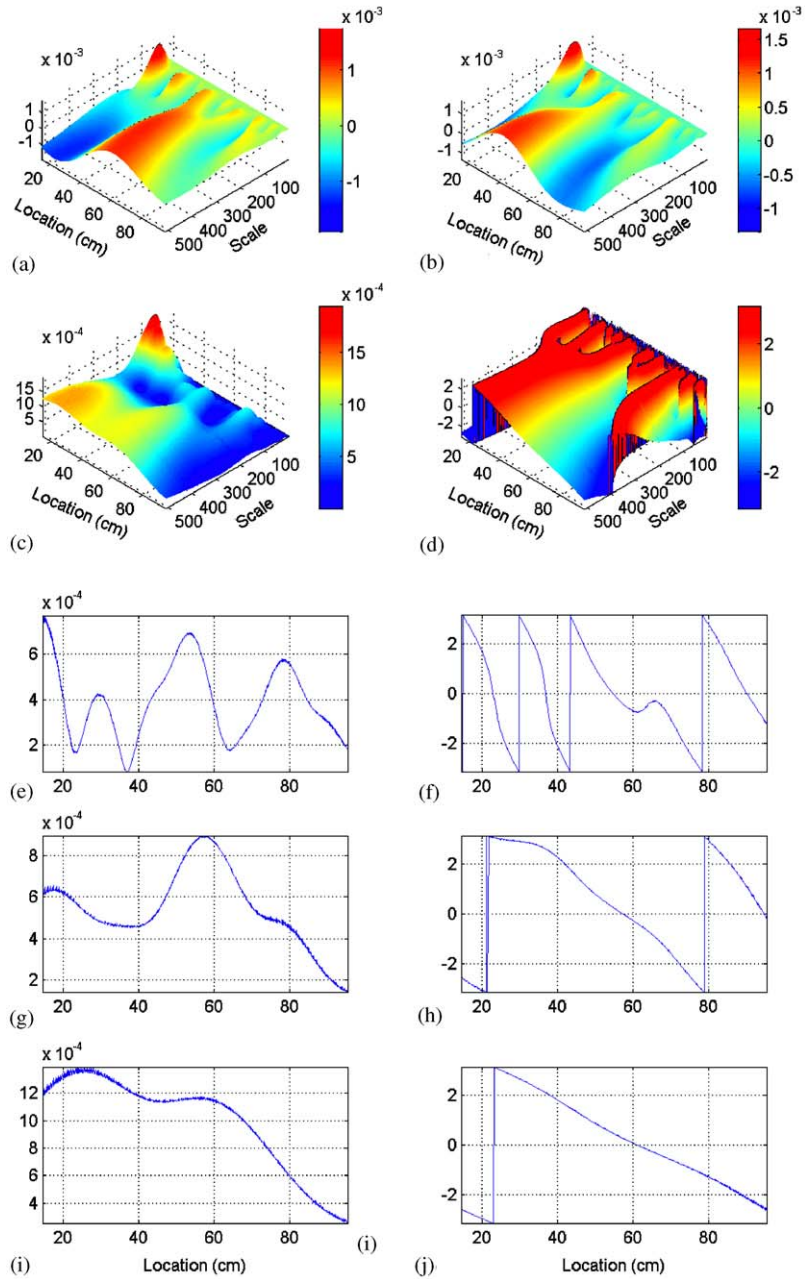
Fig. 18. Complex Gaussian wavelet coefficients of mode shape difference function between D2 and intact state: (a) real coefficients, (b) imaginary coefficients, (c) modulus of coefficients, (d) angle of coefficients, (e) modulus at $s = 150$, (f) angle at $s = 150$, (g) modulus at $s = 226$, (h) angle at $s = 226$, (i) modulus at $s = 452$, and (j) angle at $s = 452$.
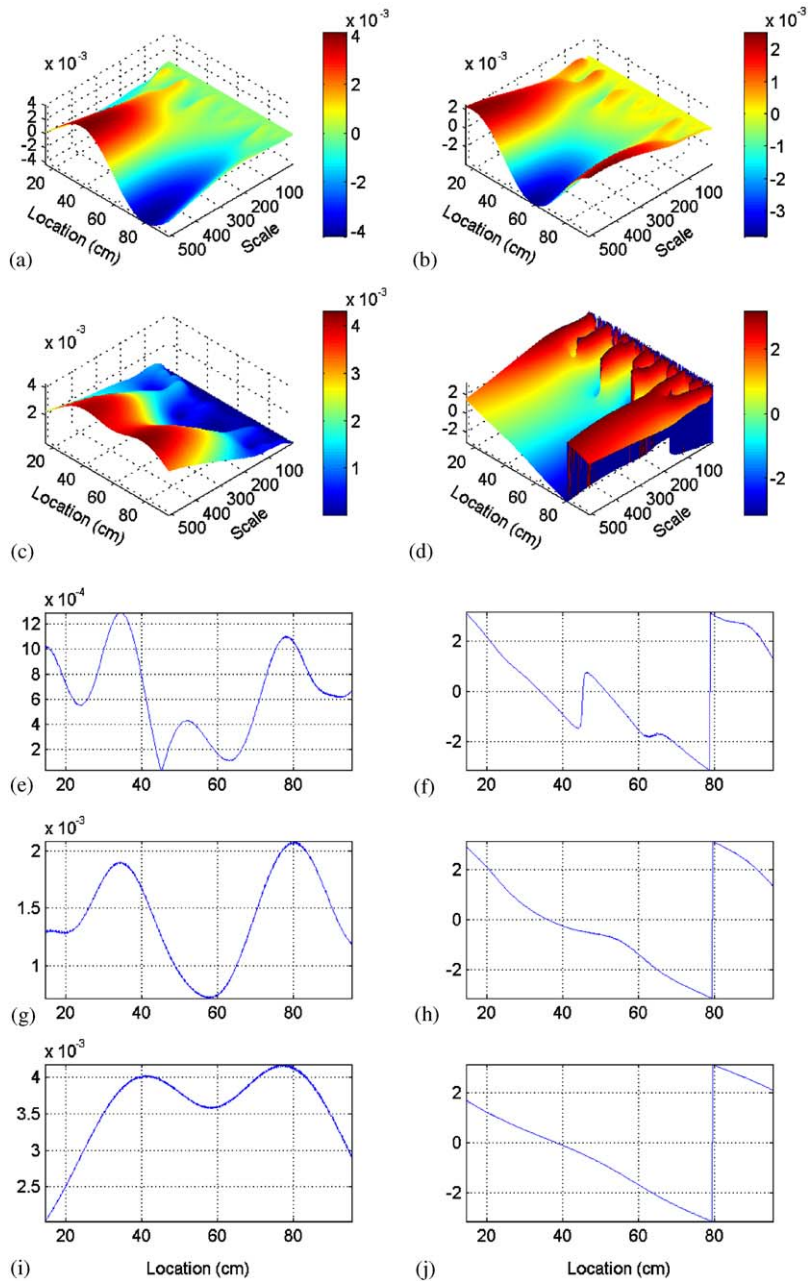
Fig. 19. Complex Gaussian wavelet coefficients of mode shape difference function between D2 and D1 damaged states: (a) real coefficients, (b) imaginary coefficients, (c) modulus of coefficients, (d) angle of coefficients, (e) modulus at $s = 150$, (f) angle at $s = 150$, (g) modulus at $s = 226$, (h) angle at $s = 226$, (i) modulus at $s = 452$, and (j) angle at $s = 452$.

introduced as the index of structural health. For damage location identification the mode shape difference function is subjected to second-order complex continuous Gaussian wavelet transformation. The results have been successfully used in detecting damages and their locations despite noise in the measured data.

Acknowledgements

Appendix A

Least-Square Curve Fitting Method of Optimization
The least-square fitting method is implemented using the following procedure:
(1) Estimate an initial vector for the unknown parameters.

$$\vec{V}_k \text{ at } k=0 \Rightarrow \vec{V}_0 = \begin{Bmatrix} P_0 \\ Q_0 \\ R_0 \\ h_0 \\ k_0 \\ a_0 \end{Bmatrix} \tag{A.1}$$

(2) Find $\Delta(\vec{V}_k)$ using Eqs. (6) and (5).
(3) Find the gradient vector of Δ at $\vec{V}_k$ as

$$\vec{g} = \frac{\partial \Delta(\vec{V}_k)}{\partial \vec{V}} \Rightarrow \vec{g} = \begin{Bmatrix} \frac{\partial \Delta(\vec{V}_k)}{\partial P} \\ \frac{\partial \Delta(\vec{V}_k)}{\partial Q} \\ \frac{\partial \Delta(\vec{V}_k)}{\partial R} \\ \frac{\partial \Delta(\vec{V}_k)}{\partial h} \\ \frac{\partial \Delta(\vec{V}_k)}{\partial k} \\ \frac{\partial \Delta(\vec{V}_k)}{\partial a} \end{Bmatrix} = \sum_i \sum_j 2[G(i,j) - \tilde{G}(i,j)] \begin{Bmatrix} \frac{\partial G(i,j)}{\partial P} \\ \frac{\partial G(i,j)}{\partial Q} \\ \frac{\partial G(i,j)}{\partial R} \\ \frac{\partial G(i,j)}{\partial h} \\ \frac{\partial G(i,j)}{\partial k} \\ \frac{\partial G(i,j)}{\partial a} \end{Bmatrix} \tag{A.2}$$

(4) Find the Hessian matrix of Δ at $\vec{V}_k$ as

$$[H] = \frac{\partial^2 \Delta(\vec{V}_k)}{\partial \vec{V}^2} \Rightarrow [H] = \begin{bmatrix} \frac{\partial^2 \Delta(\vec{V}_k)}{\partial P^2} & \frac{\partial^2 \Delta(\vec{V}_k)}{\partial P \partial Q} & \cdots & \frac{\partial^2 \Delta(\vec{V}_k)}{\partial P \partial a} \\ \frac{\partial^2 \Delta(\vec{V}_k)}{\partial P \partial Q} & \frac{\partial^2 \Delta(\vec{V}_k)}{\partial Q^2} & \cdots & \frac{\partial^2 \Delta(\vec{V}_k)}{\partial Q \partial a} \\ \vdots & \vdots & \cdots & \vdots \\ \frac{\partial^2 \Delta(\vec{V}_k)}{\partial P \partial a} & \frac{\partial^2 \Delta(\vec{V}_k)}{\partial Q \partial a} & \cdots & \frac{\partial^2 \Delta(\vec{V}_k)}{\partial a^2} \end{bmatrix} \tag{A.3}$$

(5) Find "S" in the following equation so that Δ is minimized

$$\vec{V}_{k+1} = \vec{V}_k - S[H(\vec{V}_k)]\vec{g}(\vec{V}_k) \tag{A.4}$$

(6) If $|\vec{V}_{k+1} - \vec{V}_k| \leqslant \varepsilon$, where ε is a predetermined small number as the criterion for convergence, then stop searching and the problem is solved. If this criterion is not met, set $\vec{V}_k = \vec{V}_{k+1}$ and go back to step 2.

The theoretical derivation for $\vec{g}$ and $[H]$ in Eqs. (A.3) and (A.4) was carried out analytically, and the optimization procedure was coded in C++. This optimization process yields edge location, slope, and curvature.

References

[1] S.W. Doebling, C.R. Farrar, M.B. Prime, D.W. Shevitz, Damage identification and health monitoring of structural and mechanical systems from change in their vibration characteristics: a literature review. Las Alamos National Laboratory Report LA-13070-MS, May 1996, Las Alamos, New Mexico.

[2] A.D. Dimarogonas, Vibration of cracked structures: a state of the art review, *Engineering Fracture Mechanics* 55 (1996) 831–857.

[3] A.A. Kassim, M.A. Mannan, M. Jing, Machine tool condition monitoring using workpiece surface texture analysis, *Machine Vision and Application* 11 (2000) 257–263.

[4] F. Lahanjar, R. Bernard, F. Pernus, S. Kovacic, Machine vision system for inspecting electric plates, *Computers in Industry* 47 (2002) 113–122.

[5] J.B. Zhang, Computer-aided visual inspection for integrated quality control, *Computers in Industry* 30 (1996) 185–192.

[6] J.C. Hsu, W.L. chen, R.H. Lin, E.C. Yeh, Estimation of previewed road curvatures and vehicular motion by a vision based data fusion scheme, *Machine Vision and Applications* 9 (1997) 179–192.

[7] K. Wiltschi, A. Pinz, T. Lindeberg, An automatic assessment scheme for steel quality inspection, *Machine Vision and Application* 12 (2000) 113–128.

[8] P.B. Chou, A.R. Rao, M.C. Sturzenbecker, F.Y. Wu, V.H. Brecher, Automatic defect classification for semiconductor manufacturing, *Machine Vision and Application* 9 (1997) 201–214.

[9] R. Aufrere, R. chapuis, F. chausse, A model-driven approach for real-time road recognition, *Machine Vision and Applications* 13 (2001) 95–107.

[10] D.G. Morgenthaler, A. Rosenfeld, Multidimensional edge detection by hypersurface fitting, *IEEE Transactions on Pattern Analysis and Machine Intelligence PAMI* 3 (1981) 482–486.

[11] R.M. Haralick, L. Watson, A facet model for image data, *Computer Graphics and Image Processing* 15 (1981) 113–129.

[12] H.D. Tagare, R.J.P. deFigueiredo, On the localization performance measure and optimal edge detection, *IEEE Transactions on Pattern Analysis and Machine Intelligence* 12 (1990) 1186–1190.

[13] J. Canny, A computational approach to edge detection, *IEEE Transaction on Pattern Analysis and Machine Intelligence PAMI* 8 (1986) 679–698.
[14] M.H. Hueckel, A local visual operator which recognizes edges and lines, *Journal of the Association for Computing Machinery* 20 (1973) 634–647.
[15] M.H. Hueckel, An operator which located edges in digitized pictures, *Journal of the Association for Computing Machinery* 18 (1971) 113–125.
[16] M.J. Brooks, Rationalizing edge detectors, *Computer Graphics and Image Processing* 8 (1978) 277–285.
[17] S.W. Zucker, R.A. Hummel, A three dimensional edge operator, *IEEE Transaction on Pattern Analysis and Machine Intelligence PAMI* 3 (1981) 324–331.
[18] R. Machuca, A.L. Gilbert, Finding edges in noisy scenes, *IEEE Transactions on Pattern Analysis and Machine Intelligence PAMI* 3 (1981) 103–111.
[19] J.S. Chen, G. Medioni, Detection, localization, and estimation of edges, *IEEE Transactions on Pattern Analysis and Machine Intelligence PAMI* 11 (1989) 191–198.
[20] V. Torre, T.A. Poggio, On edge detection, *IEEE Transactions on Pattern Analysis and Machine Intelligence PAMI* 8 (1986) 147–163.
[21] H. Ishii, T. Kimura, M. Sone, A. Taguchi, An edge detection from images corrupted by mixed noise using fuzzy inference, *Electronics and Communication in Japan* 83 (2000) 39–50.
[22] T.Y. Kim, J.H. Han, Edge representation with fuzzy sets in blurred images, *Fuzzy Sets and Systems* 100 (1998) 77–87.
[23] Z.D. Lan, R. Mohr, Direct linear subpixel correlation by incorporation of neighbor pixels information and robust estimation of window transformation, *Machine Vision and Applications* 10 (1998) 256–268.
[24] H.K. Aghajan, C.D. Schaper, T. Kailath, Machine vision techniques for subpixel extimation of critical dimensions, *Optical Engineering* 32 (1993) 828–839.
[25] A. Huertas, G. Medioni, Detection of intensity changes with subpixel accuracy using Laplacian–Gaussian masks, *IEEE Transactions on Pattern Analysis and Machine Intelligence PAMI* 8 (1986) 651–664.
[26] K. Jensen, D. Anastassiou, Subpixel edge localization and the interpolation of still images, *IEEE Transaction on Image Processing* 4 (1995) 285–295.
[27] E.P. Lyvers, O.R. Mitchell, M.L. Akey, A.P. Reeves, Subpixel measurements using a moment-based edge operator, *IEEE Transactions on Pattern Analysis and Machine Intelligence PAMI* 11 (1989) 1293–1309.
[28] A. Gentile, A. Messina, On the continuous wavelet transforms applied to discrete vibrational data for detecting open cracks in damaged beams, *International Journal of Solids and Structures* 40 (2003) 295–315.
[29] A.K. Pandey, M. Biswas, M.M. Samman, Damage detection from changes in curvature mode shapes, *Journal of Sound and Vibration* 145 (1991) 321–332.
[30] J. Chance, G.R. Tomlinson, K. Worden, A simplified approach to the numerical and experimental modeling of the dynamics of a cracked beam. In: *12th International Modal Analysis Conference*, Honolulu, USA (1994), pp. 778–785.
[31] M.M.F. Yuen, A numerical study of the eigenparameters of a damaged cantilever, *Journal of Sound and Vibration* 103 (1985) 301–310.
[32] M.M.A. Wahab, G.D. Roeck, Damage detection in bridges using modal curvatures: application to real damage scenario, *Journal of Sound and Vibration* 226 (1999) 217–235.
[33] I. Daubechies, Ten Lectures on Wavelets, CBMS-NSF Regional Conference Series in Applied Mathematics. Society for Industrial and Applied Mathematics, 1992, Philadelphia, Pennsylvania.
[34] S. Mallat, A theory for multi resolution signal decomposition: the wavelet representation, *IEEE Transaction on Pattern Analysis and Machine Intelligence PAMI* 11 (1989) 674–693.
[35] Z.K. Peng, F.L. Chu, Application of the wavelet transform in machine condition monitoring and fault diagnostics: a review with bibliography, *Mechanical Systems and Signal Processing* 18 (2004) 199–221.
[36] K.M. Liew, Q. Wang, Application of wavelet theory for crack identification in structures, *Journal of Engineering Mechanics* 124 (1998) 152–157.
[37] Q. Wang, X. Deng, Damage detection with spatial wavelets, *International Journal of Solids and Structures* 36 (1999) 3443–3468.

[38] S.T. Quek, Q. Wang, L. Zhang, K.K. Ang, Sensitivity analysis of crack detection in beams by wavelet technique, *International Journal of Mechanical Sciences* 43 (2001) 2899–2910.

[39] J.C. Hong, Y.Y. Kim, H.C. Lee, Y.W. Lee, Damage detection using the Lipschitz exponent estimated by the wavelet transform: applications to vibration modes of a beam, *International Journal of Solids and Structures* 39 (2002) 1803–1816.

[40] J. Lu, Y.T. Hsu, Vibration analysis of an inhomogeneous string for damage detection by wavelet transform, *International Journal of Mechanical Sciences* 44 (2002) 745–754.

[41] J. Ye, G. Fu, U.P. Poudel, Subpixel edge matching for digital photogrammetry. In: *Proceedings of 8th Pan American Congress of Applied Mechanics (PACAM VIII)*, Cuba, January 2004.

[42] D.J. Williams, M. Shah, Edge characterization using normalized edge detector, *Graphical Models and Image Processing* 55 (1993) 311–318.

[43] A.K. Louis, P. MaaB, A. Rieder, *Wavelets Theory and Applications. Pure and Applied Mathematics: A Wiley-Interscience Series of Texts, Monographs &Tracts*, Wiley, New York, 1997.

[44] C.K. Chui, L. Montefusco, L. Puccio, *Wavelets Theory, Algorithms, and Applications. Wavelets Analysis and its Applications*, vol. 5, Academic Press, New York, 1994.

[45] L. Debnath, *Wavelet Transforms & Time-Frequency Signal Analysis*, Birkhauser, Boston, 2001.

[46] P. Wojtaszczyk, *A Mathematical Introduction to Wavelets. London Mathematical Society Student Texts*, vol. 37, Cambridge University Press, Cambridge, 1997.

[47] L. Debnath, *Wavelet Transforms & Their Applications*, Birkhauser, Boston, 2002.

[48] MEscope Ves (VT-570), Vibrant Technology Inc., http://www.vibetech.com.